Automated analysis and visualization of preclinical whole-body microCT data

Baiker, M.

Citation
Baiker, M. (2011, November 17). *Automated analysis and visualization of preclinical whole-body microCT data*. Retrieved from https://hdl.handle.net/1887/18101

3

Atlas-Based Whole-Body Segmentation of Mice from Low-Contrast MicroCT Data

Chapter 3

Abstract

This paper presents a fully automated method for atlas-based whole-body segmentation in non-contrast-enhanced MicroCT data of mice. The position and posture of mice in such studies may vary to a large extent, complicating data comparison in cross-sectional and follow-up studies. Moreover, MicroCT typically yields only poor soft tissue contrast for abdominal organs. To overcome these challenges, we propose a method that divides the problem into an atlas constrained registration, based on high-contrast organs in MicroCT (skeleton, lungs and skin), and a soft tissue approximation step for low-contrast organs. We first present a modification of the MOBY mouse atlas (Segars *et al.* 2004) by partitioning the skeleton into individual bones, by adding anatomically realistic joint types and by defining a hierarchical atlas tree description. The individual bones as well as the lungs of this adapted MOBY atlas are then registered one by one by traversing the model tree hierarchy. To this end, we employ the Iterative Closest Point method and constrain the Degrees of Freedom of the local registration, dependent on the joint type and motion range. This atlas-based strategy renders the method highly robust to exceptionally large postural differences among scans and to moderate pathological bone deformations. The skin of the torso is registered by employing a novel method for matching distributions of geodesic distances locally, constrained by the registered skeleton. Because of the absence of image contrast between abdominal organs, they are interpolated from the atlas to the subject domain using Thin-Plate-Spline approximation, defined by correspondences on the already established registration of high-contrast structures (bones, lungs and skin).

We extensively evaluate the proposed registration method, using 26 *non-contrast-enhanced* MicroCT datasets of mice, and the skin registration and organ interpolation, using *contrast-enhanced* MicroCT datasets of 15 mice. The posture and shape varied significantly among the animals and the data was acquired *in vivo*. After registration, the mean Euclidean distance was less than two voxel dimensions for the skeleton and the lungs respectively and less than one voxel dimension for the skin. Dice coefficients of volume overlap between manually segmented and interpolated skeleton and organs vary between 0.47 ± 0.08 for the kidneys and 0.73 ± 0.04 for the brain. These experiments demonstrate the method's effectiveness for overcoming exceptionally large variations in posture, yielding acceptable approximation accuracy even in the absence of soft tissue contrast in *in vivo* MicroCT data, without requiring user initialization.

Atlas-Based Whole-Body Segmentation of Mice from MicroCT data

3.1 Introduction

3.1.1 Background

MOLECULAR IMAGING modalities are nowadays regarded as powerful tools for pre-clinical (small animal) research, especially for characterization and quantification of molecular processes *in vivo* [2]. In contrast to traditional structural imaging methods in diagnostic medicine, their aim is to determine disease-related abnormalities at a microscopic (cellular) scale at an early stage and to subsequently correlate these with macroscopic anatomical changes over time [3]. This adds a new dimension to animal experiments, since the traditional cross-sectional studies using different animals can be extended to follow-up studies, using the same animal.

While sometimes researchers are interested in imaging molecular events in a specific target organ, e.g. the brain or the heart, it is often necessary to acquire data from the entire animal. This is particularly important in oncology, where researchers aim at monitoring metastatic disease, to answer questions like where in the body particular tumor cells metastasize, and to follow tumor growth and interaction with its environment [5,6]. Bioluminescence Imaging (BLI) and Fluorescence Imaging (FLI) are useful modalities for this purpose because of their high sensitivity but in general do not provide anatomical reference information. Therefore, BLI or FLI datasets are often combined (fused) with high-resolution diffuse light photographs and coregistered MicroCT datasets. Although we earlier demonstrated that this improves visual data navigation [7], the localization of a particular structure of interest remains challenging if the structure of interest does not show sufficient contrast, for instance for abdominal organs in MicroCT. An automated whole-body segmentation of the entire animal, including the skeleton, would therefore greatly facilitate data interpretation. Moreover, a whole-body segmentation can be useful to localize and quantify bioluminescence sources, because accurate Bioluminescence Tomography (BLT) approaches require a heterogeneous tissue model [90,91].

Since light propagation in tissue is highly diffusive and light has a very limited penetration depth, the positioning of the animal in the BLI and FLI data acquisition device is strongly dependent on the type of study. If there are e.g. metastases in the spine, the animal should be positioned such, that the back of the animal is directed toward the CCD camera. Therefore, the data acquisition protocol cannot be standardized and the animal posture and shape may vary significantly among different animals in a cross-sectional study or the same animal in a follow-up study. The reason is that an animal body consists of many individual (rigid) bones next to multiple (nonrigid) organs and other soft tissues, which renders the animal interior largely heterogeneous. Besides the shape variability of these individual parts, there exists an additional variability in location relative to each other, which is especially the case for the distal parts of the skeletal system (limbs). Above that, being the modality of choice for bone imaging, non-contrast-enhanced MicroCT shows poor soft tissue contrast (Fig. 1.3, right). This complicates data comparison, especially in the abdominal cavity.

The goal of this work is to provide a fully automated, atlas driven method for whole-body segmentation of mice. To deal with follow-up as well as cross-sectional data, the
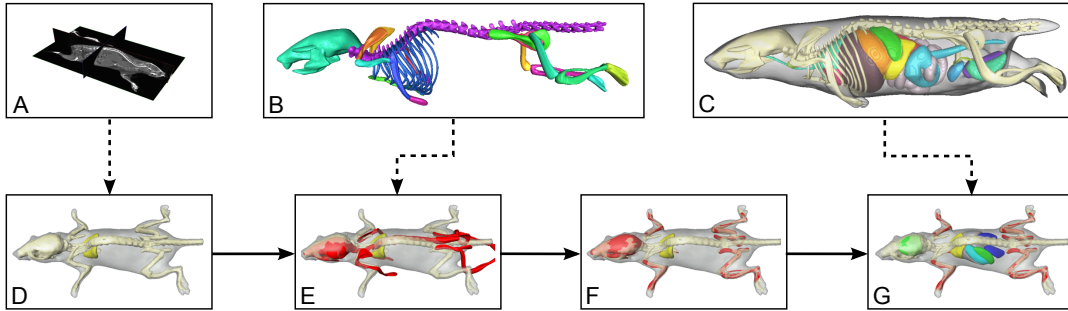
Figure 3.1: Overview of the registration and organ approximation process. First, high contrast structures (the skeleton, the skin and the lungs) are extracted from the CT data of a given subject (A). Subsequently the atlas skeleton (B) and lungs and the extracted skeleton and lungs (D) are registered (E and F) using an anatomically realistic kinematic model. Finally, major organs are mapped from the atlas (C) to the subject domain (G). (The dashed arrows indicate the data input i.e. the CT data and the atlas).

method should be able to handle anatomical intersubject data and exceptionally high variability in posture and shape between timepoints and individuals. Moreover, the method should be robust with respect to moderate bone malformations (e.g. as a result of metastatic activity) and with respect to low soft-tissue contrast. Primary application in this paper is non-contrast-enhanced MicroCT data, acquired *in vivo*.

3.1.2   Related work

The amount of Degrees of Freedom (DoF) that a registration method has to resolve is related to the shape variability of the registration object and can become very large for nonrigid structures. A generic whole-body registration approach not only has to deal with a large shape variability of individual parts of the body, but in addition with the large postural variability of the entire body. This requires a tradeoff between an enormous amount of DoFs and deformation constraints to ensure that the individual elements of the body are transformed in an anatomically realistic way, e.g. stiff structures like bones should not be deformed as much as soft tissue structures.

Methods that aim at registration of individual anatomical structures have been extensively surveyed in the literature [12–15]. Therefore in the following, only registration strategies that are suitable to handle objects with inherent structural diversity and methods, specifically tailored for small animal whole-body registration, are reviewed.

Several strategies have been reported to tackle the aforementioned difficulties of whole-body registration. There are basically two types of approaches:

1. Methods that solve for a global transformation function directly [20, 26] and

2. Methods that are based on a set of local transformations, derived using (hierarchical) block-matching [18] or using an underlying anatomical model [32, 33, 35]. The global transformation is subsequently determined by combining the local transformations.

Atlas-Based Whole-Body Segmentation of Mice from MicroCT data

Chaudhari *et al.* [20] determine a diffeomorphic transformation between the skin surface of the Digimouse 3D atlas [36] and a subject skin, derived from MicroCT data. They segment the animal interior by surface-constrained warping of the atlas volume to the subject using harmonic maps, based on the skin mapping result. The method to a certain extent handles variations in limb position by manually drawing curves on the limbs, but does not take internal structural differences into account. Bone structures therefore can easily deform in an anatomically non-realistic way. A method that takes special care of the skeleton is presented in Li *et al.* [26]. The authors present a whole-body intersubject, intramodality (CT) approach for *ex vivo* mouse studies. They nonrigidly register centerline representations of different animal skeletons and subsequently use the correspondences to define a Thin-Plate-Spline (TPS) mapping. As a final step, they apply an intensity-based nonrigid registration. Their work is based on the skeleton and therefore distinguishes between bone and soft tissue in general. However, there is no further identification of soft tissue parts. Above that, the point matching method cannot handle large limb articulations.

A way to take local differences in tissue properties into account during registration are block-matching methods. Depending on the target, the transformation model can be adjusted to fit the deformations locally. Approaches have been presented for various applications allowing translation only [28], translation and rotation [29] or affine [30, 31] local transformations. Kovacevic *et al.* [18] apply a hierarchical block-matching method for whole-body, intramodality registration of MRI data, using locally affine transformations. The approach is based on the "part-of" concept, i.e. they first separate the main organ compound and refine that division as the registration progresses, down to single bones and organs. A drawback of block-matching methods reported in the literature is that, although the individual transformations are initialized by the registration result on a higher hierarchical level, the individual blocks are determined anatomically independent of each other. Therefore larger postural differences will lead to suboptimal results.

To deal with larger postural differences, several authors perform local registrations by integrating anatomically realistic motion constraints. Martín-Fernández *et al.* [32, 92] for example make use of an anatomical hand model to register 2D radiographs. The bones are thereby represented by a wireframe where individual 'rods' are registered imposing kinematic constraints. Du Bois d'Aische *et al.* [33] register a human head, based on a model of the cervical spine. Articulated vertebrae are registered to the target image and the deformation is propagated to the rest of the head using a linear elastic model. Papademetris *et al.* [35] use a kinematic model to register the legs of a mouse by modeling the joints. Articulated parts thereby have to be segmented manually. After registration, they propagate the deformations to soft tissue parts by focusing on the folding problem at interfaces of articulated parts. Although they show the applicability of such an approach for small animal registration, they focus on a subpart of the body.

In summary, some available methods can be used either for whole-body applications, as long as differences in posture and shape are small. Some authors use animal holders or place the animals in a similar position for each scan. Other methods include *a priori* information, for instance about structural properties of single elements of the object, about kinematics of elements relative to each other or about position and spatial extent of

anatomical objects but again, allow small articulations only or were used for registration of subparts of a body. Often the method is only suitable for intramodality applications [18, 26] and registration is therefore restricted to image features that show sufficient contrast in the used modality. The required amount of user interaction e.g. to define joint locations or to generate labeled datasets [35] or computational demands [26] makes some methods laborious. Moreover, the aforementioned methods for small animal applications were evaluated either using synthetic data [18] or using only few subjects [20, 26, 35].

3.1.3 Contributions

In this work we present an automated method for whole-body segmentation of MicroCT datasets of mice using atlas-based registration. To accommodate for large postural variations between scans or animals, the DoFs in the registration are governed by realistic kinematic constraints on the animal skeleton in a coarse-to-fine manner: after global alignment, individual bones are registered locally, subject to a hierarchical model of the skeleton that includes anatomically realistic motion constraints in the joints. The registration is driven by high-contrast anatomical structures (bones, lungs and skin) included in the matching hierarchy. To compensate for missing registration features in MicroCT (most organs and soft tissue), we rely on a publicly available whole-body mouse atlas (the MOBY atlas [59]). Abdominal organs with low contrast are estimated using Thin-Plate-Splines (TPS) interpolation [80], after establishing a dense set of correspondences between the high-contrast structures in the data and the atlas.

The novel elements in this work are:

- We extend the MOBY atlas by partitioning the static skeleton into individual bones, and defining anatomically realistic kinematic constraints for each joint.

- We define a hierarchical anatomical model of the animal body for automated registration of the MOBY atlas.

- We describe a novel algorithm to determine dense correspondences on the animal skin based on an initial set of sparse correspondences, using matching of local distributions of geodesic distances.

- We validate our approach using 41 MicroCT datasets of mice scanned in arbitrary posture. To the best of our knowledge this represents the most extensive validation reported for whole-body small animal segmentation.

Pilot studies on the methods in this work were presented previously [86, 93].

3.2 Methodology

An overview of the presented approach is given in Fig. 3.1. First the anatomical atlas modifications (Fig. 3.1, B) as well as the hierarchical anatomical model are introduced
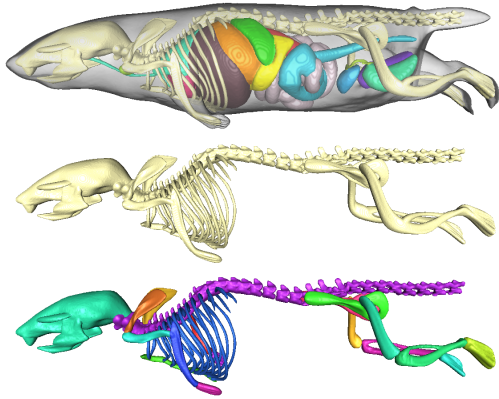
Figure 3.2: *The mouse atlas (top), the skeleton as originally included in the atlas (middle) and after segmentation of individual bones (bottom). The colors indicate different bones.*
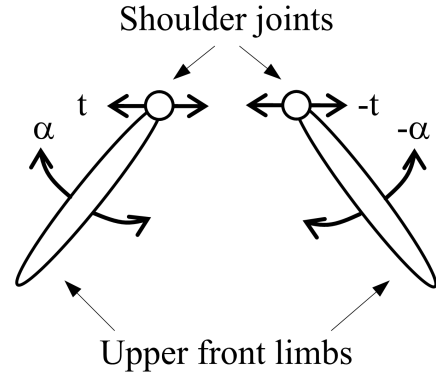

Figure 3.3: *Representation of the shoulder complex. Besides global DoFs, a symmetric translation t and rotation α with respect to the shoulder joints are allowed.*

(section 3.2.1). Details about the automated extraction of the high-contrast organs (skeleton, lungs and skin) are given in section 3.2.2 (Fig. 3.1, D). Next, the registration of the individual parts of the hierarchy, namely the global registration of the entire skeleton (Fig. 3.1, E) and the local registration of individual structures (Fig. 3.1, F) are given in section 3.2.3. The determination of skin correspondence is introduced in section 3.2.4 and section 3.2.5 describes how skeleton, lung and skin correspondence is used for low-contrast organ interpolation (Fig. 3.1, G).

3.2.1 Atlas adaptations and anatomical model definition

The atlas used in this work was originally developed by Segars *et al.* [59]. It is a 4D whole-body anatomical mouse model including bones and organs that allows to simulate breathing and heart motion. For this work, an instance of the model was generated at a fixed time point in the respiratory and cardiac cycle at end diastole and full exhale (Fig. 3.2, top). The skeleton is represented as a whole and does not distinguish between individual bones (Fig. 3.2, middle). To integrate rotational DoFs in the joints, we segmented the individual bones using Amira 3.1 (Mercury Computer Systems, Chelmsford, USA), guided by anatomical text books [76, 77], yielding a labeled volume dataset with voxel size 90 μm $\times$ 90 μm $\times$ 90 μm. Subsequently, triangulated surface representations of all bones, the organs and the skin were generated using the Marching Cubes Algorithm [94]. A surface representation of the segmented skeleton is given in Fig. 3.2 (bottom). Based on the segmented bones and lungs, a set of characteristic anatomical landmarks at distinctive locations like the joint pivot points, the caudal end of the skull etc. was defined manually on the surfaces and the skin surface was partitioned into torso and limbs. Second, local coordinate systems for each bone were defined such that the realistic bone articulation for each joint could be expressed more intuitively, e.g. the knee rotation axis and the longitudinal axis of the tibia were chosen to be coordinate axes of
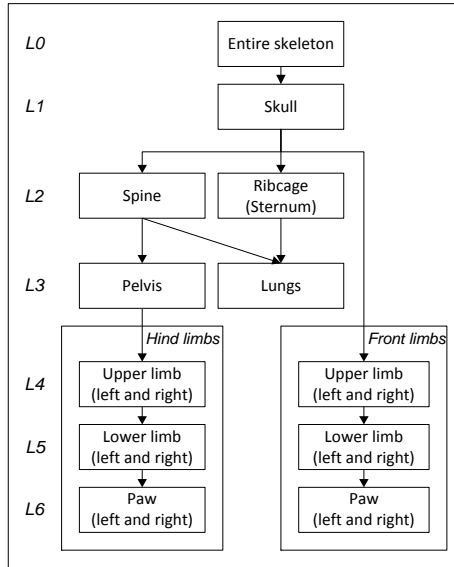
Figure 3.4: Hierarchical anatomical tree for the skeleton and the lungs. The connections depict relations between single bones or bone compounds such that a part on a lower level is initialized by the registration result on a high level.

the local coordinate system.

Three types of joints were distinguished: ball joints, hinge joints and the shoulder complex (both shoulders combined). Tab. 2.1 shows the DoFs for the ball and hinge joints. Due to the large number of DoFs in the shoulder, an additional motion constraint was introduced by allowing only a coupled, symmetric displacement of both front upper limbs, with a varying distance between the shoulders and a rotation toward and away from each other (Fig. 3.3). Subsequently, the left and the right front upper limbs are decoupled. The hierarchical anatomical tree of the animal skeleton and the lungs is shown in Fig. 3.4, containing the bones that determine the major posture variations. For capturing the animal posture, smaller skeletal elements such as the shoulder blades and individual paw bones were excluded. Assuming that the spine and the sternum sufficiently describe the global pose of the ribcage, individual ribs were removed from the data by applying appropriate preprocessing steps (see section 3.3.1), as indicated in Fig. 3.5. In principle, each of the 23 individual vertebrae in the mouse body could be separately modeled. However this would greatly increase the total amount of DoFs. To avoid this, we opted for modeling the spine as a 3D curve connecting the skull to the pelvis.

3.2.2   Robust extraction of registration features

The presented registration method relies on automatically extracting surface meshes of the high-contrast organs from MicroCT data (skeleton, skin, lungs), and several interchangeable processing pipelines can be envisioned that produce these meshes automatically. We opted for extracting these meshes by smoothing the CT data to remove noise and small skeletal elements, followed by isodata thresholding (Ridler *et al.* [95]). The
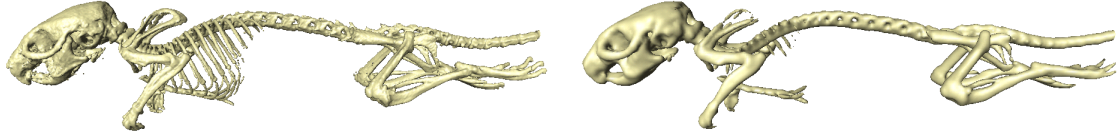
Figure 3.5: Isosurfaces of a mouse skeleton before (left) and after preprocessing (right).

resulting data volume was used for global skeleton alignment and spine determination, as described in section 3.2.3. The skin boundary of the animal was segmented from the smoothed data volume by isodata thresholding in one iteration (threshold t_1). For segmentation of the lungs, the triangle algorithm [96] was selected for its ability to classify lung tissue voxels in the absence of a clear lung peak in the MicroCT histogram . The required parameters were set to $b_{min} = t_1$ and b_{max} being the bin k of the 8-bit histogram h_{gray} where $h_{gray}(k > t_1)$ is maximal. Triangular surface meshes were extracted from the segmented volumes using the Marching Cubes Algorithm [94]. For the determination of the skin correspondences, the skin surfaces were simplified using the QSlim method by Garland *et al.* [97].

3.2.3 Registration of high-contrast organs

To initialize the hierarchical model registration, first a coarse alignment of the atlas and the target data on the highest hierarchical level ($L0$), i.e. the entire mouse skeleton, is performed. For this purpose, a similarity transformation model with seven DoFs is employed (translation, rotation, isotropic scaling), which suffices to accommodate for the animal pose in the CT scanner and for size differences between animals. The individual DoFs are resolved in several steps, which are based on a set of robust inherent features of the skeleton:

- Alignment of the anteroposterior axis of the animal, based on the Center of Gravity (CoG) and the first eigenvector of the skeleton, represented as a 3D point set, using Principal Component Analysis [98].

- Determination of the animal position (prone/supine) in the scanner, using a 3D curve representation of the skeleton. This is derived from the labeled skeleton volume by binning the data along the anteroposterior axis and calculating the CoG in each bin. Between the ribcage and the pelvis, the curve closely follows the spine. The course of the curve in this part allows deriving the animal position.

- Determination of the animal orientation, because the amount of bone is much larger in the cranial half.

- Determination of the neck location, based on the projection of the 3D curve to the coronal plane.

- Derivation of an initial scale factor from the total bone content of the skeletons.

An example of the result of the global alignment step is given in Fig. 3.8 (top row).

Following the coarse alignment of the entire skeleton, lower hierarchical tree levels are registered piece by piece. For the individual bones, transformation models according to Tab. 2.1 are used. We consider the amount of DoFs to be sufficient to model coarse anatomical bone differences among subjects. Adding more DoFs would lead to more accurate registration results but would compromise robustness with respect to large postural variations, especially if bones show pathological changes.

The transformation parameters for the individual bones are determined using the Iterative Closest Point (ICP) algorithm (Besl *et al.* [79]). It is a method that iteratively solves for transformation and correspondence, by minimizing the Euclidean distance between two point sets. Because of the restricted amount of DoFs of the individual transformations and the fact that a skeleton segmentation from CT data contains only few outliers, ICP offers the best tradeoff between robustness and computational burden for the problem at hand and therefore a more robust but more expensive method, e.g. the Robust Point Matching (RPM) framework [99], is not required. While ICP has originally been developed for incorporating rigid transformations only, non-isotropic scaling can be integrated as well. In this way, it is possible to account for anatomical intersubject variability in bone thickness and length.

The articulated registration of the skeleton is performed by traversing the hierarchical anatomical tree (Fig. 3.4) in a top-down manner i.e. starting at $L1$ and proceeding to the lowest level $L6$. At each step ICP is applied to the distal part of a joint, constrained by the respective joint type i.e. if e.g. the pelvis ($L3$) has been registered, the upper hind limb ($L4$) is registered subsequently, allowing the DoFs of a ball joint. The lungs ($L3$) are initialized based on the spine and the sternum. They are registered allowing 9 DoFs because during breathing, lungs expansion with respect to the longitudinal body axis differs significantly from the lateral expansion [100]. Elastic deformations are not modeled. After convergence of a structure, the final transformation function is used to initialize the registration of a bone at a lower hierarchical level. An example of the gradually improving overall registration error during stepwise registration of individual structures is given in Fig. 3.6.

Given the source point sets $X_k = \{x_{ki}, i = 1, 2, \ldots, M_k\}$ of the segmented atlas bones, the target point set $Y = \{y_j, j = 1, 2, \ldots, N\}$ of the skeleton segmented from CT, and the error measure E_k, the Euclidean distance between a source and the target surface, the registration is done as follows (note that X_k and Y are represented in homogeneous coordinates to enable matrix multiplications:

1: Determine the global transformation matrix T_0 that coarsely aligns the skeletons
2: **for** All k elements (bones and lungs) in the hierarchy **do**
3:     Obtain the local transformation matrices $T_1, \ldots, T_{k-1}$ of the elements on the higher levels in the hierarchy
4:     Define the parameter vector Θ_{init} for the current element
5:     Determine the transformation matrix $T_{local2global}$ that aligns the local to the global coordinate system
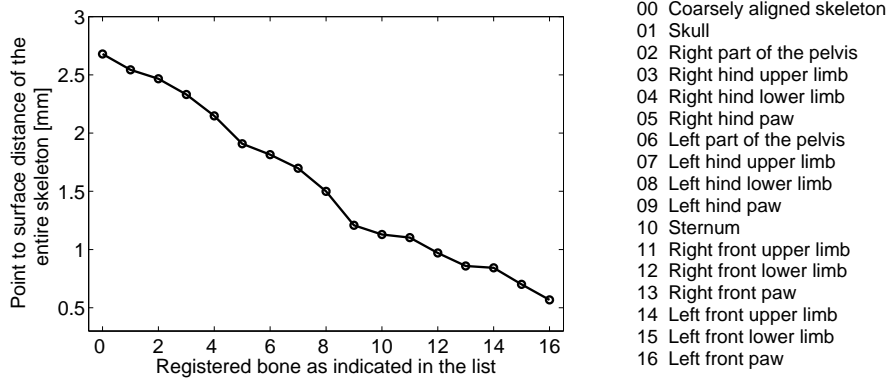6:   Apply the ICP algorithm to the current element:
7:     **repeat**

Figure 3.6: Improvement of the error criterion as the registration progresses down the anatomical tree (1voxel≙332 μm).

8:     Define $\Theta_k = \Theta_{init}$ in the first or $\Theta_k = \Theta_{new}$ in subsequent iterations

9:     Determine the local transformation matrix $T(\Theta_k) = Trans(\Theta_k)*Rot(\Theta_k)*S(\Theta_k)$

10:     Determine the global transformation matrix $T_{total}(\Theta_k) = T^{-1}_{local2global} * T(\Theta_k) * T_{local2global} * T_{k-1} * \ldots * T_1 * T_0$ and transform the current element

11:     Calculate the error between the source and the target:

$$E(X, Y, T_{total}(\Theta_k)) =$$
$$\frac{1}{M_k} \sum_{i=1}^{M_k} \min_{j=1\ldots N} (\|y_j - T_{total}(\Theta_k) * x_{ki}\|) \tag{3.1}$$

12:     Search for another set of parameters Θ_{new} that yields a smaller error, using a trust-region approach that is based on the interior-reflective Newton method [101]

13:     **until** $|\Theta_k - \Theta_{new}| \leq \epsilon$, with ϵ being the user defined parameter tolerance

14: **end for**

The spinal centerline is extracted using three dimensional region growing, where a landmark at the skull-atlas connection serves as the seed point and the region growing is stopped when the vertebra connecting the spine to the pelvis is reached. The 26 intervertebra connections are subsequently mapped from the atlas to the subject, relative to the length of the spine.

3.2.4   Determination of skin correspondence

Because of the high variability of animal positioning during data acquisition, the shape of the animal skin surface may have high rotational symmetry with respect to the anteroposterior body axis (Fig. 3.1, C) and may be symmetric to the sagittal (Fig. 3.7) or the transverse plane. However, one can exploit the already registered skeleton and lungs to remove postural ambiguity, and thus derive a sparse set of correspondences on

the skin to provide landmark support over the entire animal surface [102,103]. Following the skeleton registration, the manually defined landmarks in the atlas reference frame can be mapped to the target domain. As a result, the location of the atlas-annotated landmarks is known in the target domain as well. Since bone is adjacent to the skin at many locations in the animal body, an equal amount of skin correspondences can be derived by selecting the skin points closest to the bone and lungs landmarks. This sparse set of skin correspondences can only provide landmark support in regions where bones are present e.g. near to the spine. To determine a dense set of correspondences on the skin, a method is needed that handles abdominal deformations and articulated limbs.

Available methods that determine shape correspondence in the spatial domain, for example the RPM framework, have to include a transformation model to handle large nonlinear deformations. Another approach is to represent the shape intrinsically. This can be done e.g. by using Euclidean distances between points [104], rendering the representation invariant to rigid body transformations or by using geodesic distances (the shortest path between two points on a manifold), to obtain invariance to rigid body transformations and bending [105]. Using appropriate normalization of the representations, invariance to scaling can be obtained as well.

Elad *et al.* [105] used a bending invariant shape signature for classifying articulated shapes and Jain *et al.* [106] aimed on determining correspondence between articulated shapes. Both methods are based on global shape representations and therefore require a very densely sampled surface. This is necessary to ensure that the larger geodesic distances can be computed accurately. However, calculating a geodesic distance distribution for each node on a dense mesh is very time consuming. Given an initial set of correspondences on the surface it is possible to use a more local shape representation based on geodesic distances. This has the advantage of a reduced calculation time and that local shape variations are better represented. Above that, it is possible to use a coarser mesh sampling [107], which further reduces computational burden.

Our approach employs an intrinsic representation of the skin shape that is based on geodesic distances. We assume that elastic deformations i.e. stretching or compression of the skin play a minor role and that bending is the main form of deformation. We determine correspondence between two shapes by calculating distributions of geodesic distances locally, starting from the initial set of correspondences, and continue until the entire surface is covered. A method that is similar to ours was presented by Wang *et al.* [108], but their method requires a much larger set of initial correspondences.

Matching of local geodesic distributions

Given an initial sparse set of corresponding nodes on the source and the target surface, we determine new correspondences in the vicinity of each node in this sparse set, yielding an extended set of correspondences. The vicinity of a node is controlled by two fixed neighborhood parameters: a minimum distance g_{min}, to prevent that new correspondences are too close to already known correspondences and a maximum distance g_{max}, to ensure locality. (Details on the determination of the geodesic distances are given in the 'Appendix'). Subsequently, more correspondences are determined in the vicinity of the extended set and so on. The search for correspondences stops when there are no new

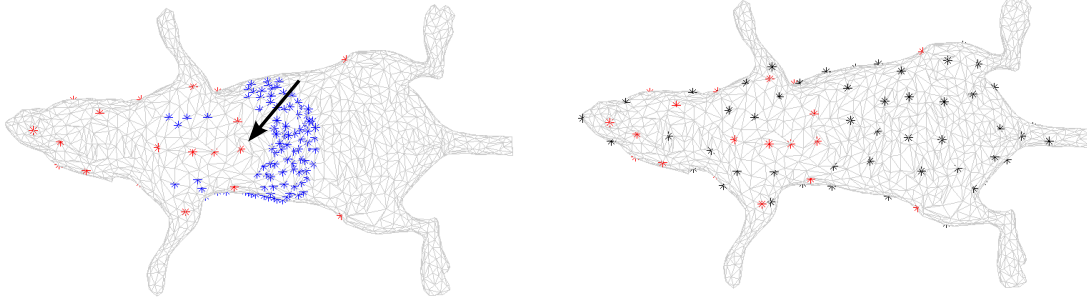# Atlas-Based Whole-Body Segmentation of Mice from MicroCT data

Figure 3.7: The images show an example skin surface in bottom view. Depicted are an initial sparse landmark set (red stars) and candidates for new correspondences (blue stars), based on a known landmark (arrow) on the chest (left). The final dense set of correspondences is indicated by black stars (right).

candidates left on the mesh. Parameter K controls how many already known correspondences are taken into account to derive the distribution of geodesic distances. To find optimal parameter values, g_{min} and g_{max} were fixed and K was determined as a tradeoff between the quality of the mapping and the processing time. The quality investigation was based on the mean distance between the source and the target skin surfaces, after determining correspondence and mapping the source to the target surface (mapping details are given in section 3.2.5) and on a triangle quality measure.

Let $P = \{p_i, i = 1, 2, \ldots, m\}$ and $Q = \{q_j, j = 1, 2, \ldots, n\}$ be the nodes of respectively the target and source surfaces to be matched, g_i and g_j be the geodesic distances between two nodes on P and Q and $h_i(k)$ with $k = 1, 2, \ldots, K$ and $h_j(k)$ with $k = 1, 2, \ldots, K$ be a distribution of local geodesic distances for the nodes $p_i \in P$ and $q_j \in Q$ based on K known correspondences on the surface. So $h_i(k)$ contains the geodesic distances from node p_i to K other nodes of P, in the vicinity of p_i and $h_j(k)$ contains the geodesic distances from node q_j to K nodes of Q, in the vicinity of q_j.

1: Determine geodesic distances for each node on the target surface to the remaining nodes (for the atlas skin surface, this calculation only has to be done once).
2: Initialize a list with the initial sparse set of corresponding nodes. (Shown as red stars in Fig. 3.7, left)
3: **repeat**
4:     Select possible candidates for new correspondences on P and Q in a surface area of interest with respect to the next element on the list with $g_{max} > g_i > g_{min}$ and $g_{max} > g_j > g_{min}$. (Blue stars in Fig. 3.7, left)
5:     Calculate $h_i(k)$ and $h_j(k)$ for all possible candidates in P and Q
6:     **repeat**
7:         Calculate the cost C_{ij} for matching two nodes p_i and q_j by using the χ^2 test statistic [104]:

$$C_{ij} = \frac{1}{2} \sum_{k=1}^{K} \frac{[h_i(k) - h_j(k)]^2}{h_i(k) + h_j(k)} \tag{3.2}$$
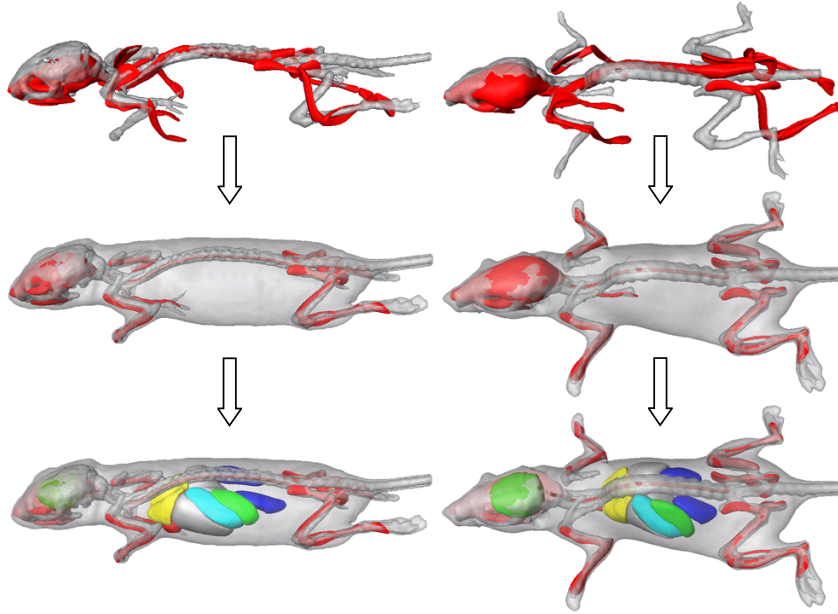
45

Figure 3.8: Registration results between the atlas (red) and two different subjects (gray) after coarsely aligning the skeleton (top), after the articulated registration (middle) and after organ interpolation (bottom).

8:      Find the best match $C_{min} = \min\limits_{i,j}(C_{ij})$

9:      Add the nodes p_{Cmin} and q_{Cmin} to the list of correspondences

10:     Remove landmark candidates around p_{Cmin} and q_{Cmin} if $g_i \le g_{min}$ or $g_j \le g_{min}$

11:   **until** No landmark candidates are left on P

12: **until** No new elements in the correspondence list are left

An example of a mouse skin surface with a dense net of correspondences is shown in Fig. 3.7 (right).

3.2.5   Atlas organ interpolation

The established point correspondences (landmarks) on bone, lungs and skin provide sufficient data support to constrain a nonrigid mapping of organs from the atlas domain to the subject domain for the entire body. For this purpose, we chose Thin-Plate-Spline (TPS) interpolation [80, 109] because correspondences can be distributed non-uniformly within the image domain and the transformation can be determined analytically.

A TPS transformation is based on the combination of a set of radial basis functions (RBF) whose coefficients determine the displacement field. RBFs are functions of the Euclidean distance between an interpolation point $\mathbf{x}$ and a landmark point $\mathbf{x}_i$, based on a kernel $R_i = R(|\mathbf{x} - \mathbf{x}_i|)$. The RBF for TPS interpolation has the form:

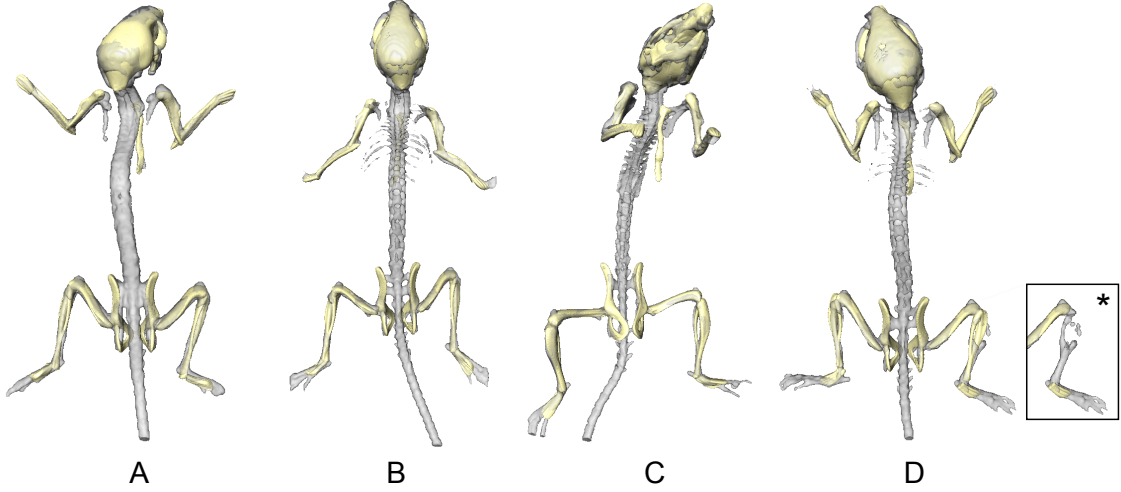$$f(\mathbf{x}) = \sum_{i=1}^{n} w_i R_i \qquad (3.3)$$

Figure 3.9: Several examples of skeleton registration results. The subject skeletons are shown in gray and the atlas bones in yellow. Three mice were in prone (A, B, D) and one mouse in supine position (C) respectively. The last example shows the result of an additional experiment to demonstrate the robustness of the method with respect to moderate bone resorption. The tibia without the registered bone is shown in the framed box (*).

with in 3D, $R_i = |\mathbf{x} - \mathbf{x}_i|$ [110], n is the amount of landmarks and w_i are the coefficients.

TPS interpolation also includes a global, linear (affine) component and so the TPS transformation $\mathbf{u}$ is determined as:

$$\mathbf{u}(\mathbf{x}) = \mathbf{A}\mathbf{x} + \mathbf{B} + \sum_{i=1}^{n} w_i R_i \qquad (3.4)$$

$\mathbf{A}$ and $\mathbf{B}$ are coefficient matrices of the affine part of the transformation.

In its original form, TPS interpolation maps a set of source points $\mathbf{p}_i$ to their corresponding target points $\mathbf{q}_i$, with $i = 1, \ldots, n$, exactly. The smoothness of the interpolation is ensured because the transformation $\mathbf{u}$ minimizes an energy functional J_{TPS} that represents the bending energy of $\mathbf{u}$ [80]. However, exact landmark matching implies that the landmark locations should be known exactly, especially for landmarks that are in close proximity to each other, to ensure that the transformation remains invertible. In our case, a node on the target skin, with a specific distribution of geodesic distances, may not have an exact match on the source skin because of the discretization of the surface. This may lead to small landmark localization errors. To deal with such errors, approximating TPS (Rohr *et al.* [111]) have been proposed. The method is similar to smoothing TPS [109] but has the advantage that a localization uncertainty can be added for each landmark individually. This is formulated into an energy functional J_λ, where J_{TPS} is incorporated by means of a regularization parameter λ:

$$J_\lambda(\mathbf{u}) = \frac{1}{n} \sum_{i=1}^{n} \frac{|\mathbf{q}_i - \mathbf{u}(\mathbf{p}_i)|^2}{\sigma_i^2} + \lambda J_{TPS}(\mathbf{u}) \qquad (3.5)$$
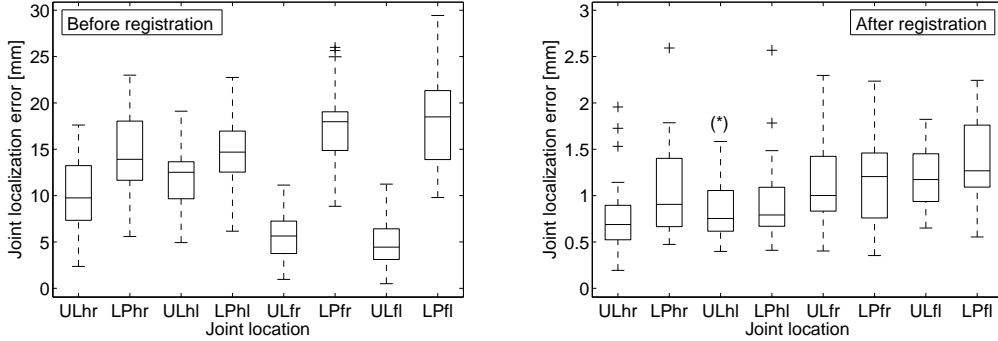
Figure 3.10: Boxplots of the joint localization errors for the limb joints (U = upper limb, L = lower limb, P = Paw, h = hind, f = front, r = right, l = left) before (left) and after the articulated registration (right). (*) There exists a joint localization error at 4.408 mm for this joint location that is not shown in the Figure (1voxel≙332 μm).

The first term measures the distance between the corresponding point sets $\mathbf{q}_i$ and $\mathbf{u}(\mathbf{p}_i)$ i.e. between n target points and n source points $\mathbf{p}_i$, mapped to the target domain by $\mathbf{u}$. Isotropic landmark localization errors can be integrated using the weighting factors σ_i, for each landmark individually. Depending on how smooth the final transformation should be, λ has to be chosen accordingly ($\lambda_{norm} = 0$: interpolation, $\lambda_{norm} = 0.1$: nearly affine transformation, $\lambda_{norm} = 0.001$: intermediate value). Like with conventional TPS, the transformation $\mathbf{u}$ of the approximating TPS can be determined analytically [111].

3.3 Experimental setup

Several experiments were executed to evaluate different aspects of the developed method. Experiments were performed on two different types of data, therefore the following sections are separated accordingly:

1. Assessment of the registration performance for the skeleton and the lungs, using *non-contrast-enhanced* data

2. Evaluation of skin landmark errors and organ interpolation performance, using *contrast-enhanced* data

3.3.1 Evaluation of skeleton and lungs registration

Data acquisition and preprocessing

For evaluation of the registration errors in skeleton and lungs, twenty-six data sets were acquired from twenty-one healthy, 6- to 10-week-old mice (Balb/c, Charles River WIGA, Sulzfeld, Germany), 20 female and 1 male, with a mean weight of 21.7g±2.2g, in prone and supine position and with arbitrary limb position. In total, 180 images were taken with step size 1°, using a Skyscan 1178 MicroCT (Kontich, Belgium), with 50keV x-ray

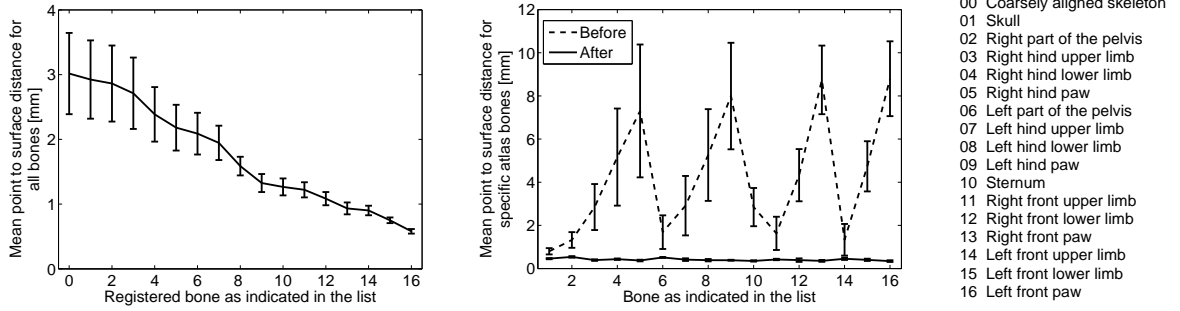## Atlas-Based Whole-Body Segmentation of Mice from MicroCT data

Figure 3.11: Overall mean error improvement during traversing the anatomical tree and mean error for specific bones before and after registration ($1voxel \hat{=} 332 \ \mu m$).

voltage, an anode current of $200\mu A$, an aluminum filter of 0.5mm thickness, an exposure time of 640ms and *without* using a contrast agent. The reconstructed datasets covered the range between -1000 (air) and +1000 (bone) Hounsfield units (HU). Neither cardiac nor respiratory gating was used.

The data with resolution 83 $\mu m \times$ 83 $\mu m \times$ 83 μm was subsampled by averaging with a factor of 4, yielding a voxel size of 332 $\mu m \times$ 332 $\mu m \times$ 332 μm, and smoothed using a Gaussian filter with kernel = 5 and sigma = 3. Subsequently, the skeleton, the skin and the lungs were segmented according to section 3.2.2. Triangular meshes were generated with $\approx$ 20000 nodes for the atlas skeleton (without ribs, spine and shoulder blades) and $\approx$ 30000 nodes for the CT skeleton surface. For skeleton registration, the set of atlas and subject surface nodes was reduced by factor 10. The lungs were represented with $\approx$ 400 nodes for the atlas and with $\approx$ 500 nodes for the CT surface.

Matching parameters

For each tree level (except $L0$), the registration was performed in two iterations. The first iteration involved was used for coarse rigid alignment allowing 6 DoFs i.e. translation and rotation in 3D, covering the entire anatomically realistic range of motion. Although not anatomically realistic for ball and hinge joints, translation was allowed to a small extent, to ensure that registration inaccuracies do not influence lower hierarchical levels. The second iteration incorporated non-isotropic scaling ($\leq 15\%$), allowing 9 DoFs. The minimization was terminated when the difference between subsequent parameter estimates was below 0.01 degrees for the rotation, 3.2 μm for the translation and 0.001 (0.1%) for the scaling parameters.

Evaluation metrics for skeleton and lung registration

To evaluate the skeleton registration performance, joint localization errors were calculated. These were expressed as the Euclidean distance between corresponding anatomical landmarks (point to point distance). To this end, the locations of the upper-lower limb and the lower limb-paw joints of all 26 data sets were indicated manually using the extracted skeleton surfaces. The difference in measured length of corresponding bones

on the right and the left side of the animal thereby gives an indication of the manual joint localization error (0.38 ± 0.25 mm, which is in the order of the data resolution). For validation, the found joint locations were compared to those determined after registration of the skeleton.

To assess the performance in areas where anatomical landmarks cannot be located manually in a reliable manner (on large parts of the bones and the lungs), the point to surface distance was determined to quantify border positioning errors, yielding an indication of the registration error of the entire object.

3.3.2 Evaluation of the skin and organ mapping

Data acquisition and preprocessing

The accuracy of the organ interpolation was determined based on datasets presented in Henning *et al.* 2008 [112]. These were acquired from fifteen healthy, 4- to 6-week-old female mice (C3H, Charles River WIGA, Sulzfeld, Germany), with a mean weight of 17.8g±0.83g, in prone position and with arbitrary limb position. The CT system was a MicroCAT II (ImTek Inc, Knoxville, TN), with 70keV x-ray voltage, an anode current of 500μA, an aluminum filter of 0.5mm thickness and an exposure time of 300-500ms. In total, 360 images were taken with step size 1° and *with injected contrast agent* Fenestra LC (ART Inc., Montreal, Canada), which is particularly suitable for increasing liver and spleen contrast. Neither cardiac nor respiratory gating was used.

Note that the contrast enhancement was only used for manual segmentation of organs to assess the performance of the organ interpolation. It was *not* used during registration as a registration feature. Although the strain of the animals in this dataset was different from the strain used for the skeleton registration validation, in our experience bone dimensions are very similar. For the femur, this has been shown in [77] (however, the density and thus the bone volume differ). For the lungs, longitudinal expansion is significantly larger for C3H mice [100].

In all the datasets the liver, the lungs and the spleen were segmented manually, based on their large contrast with respect to the surrounding tissue. The brain did not show an increased contrast but its extent is strongly restricted by the skull. Also the kidneys are not enhanced but show sufficient contrast with surrounding tissues (liver, spleen and abdominal fat deposits) for segmentation. In a subset of five datasets, the heart was also segmented, because these datasets were acquired within 30 minutes after Fenestra administration, yielding high contrast in the heart and vascular system.

To ensure the same conditions as for the skeleton registration evaluation, the data was preprocessed and the skeleton, the lungs as well as the skin were extracted in the same manner as presented in section 3.3.1. Only the subsampling parameter has been adjusted to 2, since the original resolution of the contrast-enhanced datasets was lower (107 μm $\times$ 107 μm $\times$ 107 μm).

Atlas-Based Whole-Body Segmentation of Mice from MicroCT data

Matching parameters

To determine skin correspondences, meshes were used with ≈ 7500 vertices for the atlas and ≈ 2000 vertices for the subjects. To derive the dense set of corresponding nodes, the parameters g_{min} and g_{max} were chosen such that the amount of correspondences is sufficient for the torso (relatively small surface curvature) and that almost the entire animal surface could be covered in three iterations. With $g_{min} = 15$ ($1 voxel \hat{=} 214$ μm) and $g_{max} = 50$, $K = 8$ was determined, based on the criteria described in section 3.2.4 (A detailed motivation for the selection of K is given in the 'Appendix'). The initial sparse set of correspondences was replenished by ≈ 120 nodes from the skin, all over the torso. Together with 30 correspondences on the surface of the lungs and the 32 anatomical landmarks, ≈ 182 corresponding nodes were used for mapping of the skin and major organs from the atlas domain to the subject domain. The regularization parameter for the approximating TPS was set to $\lambda = 1000$, yielding $\lambda_{norm} = \frac{\lambda}{x\_dim * y\_dim * z\_dim} = \frac{1000}{160 * 150 * 400} \approx 0.0001$ [111]. Since the initial sparse set of landmarks are considered as highly accurate, we assume a variance of $\sigma = 0.01$. All newly determined correspondences are considered as less accurate $\sigma = 2.2$ (the mean internode distance of the atlas skin surface is ≈ 5). During the experiments, the smoothness of the mapping was monitored using the determinant of the Jacobian of the final transformation, which was positive in all cases (more details are presented in the 'Appendix').

Fig. 3.8 shows two examples of mice with registered skeleton and approximated organs.

Evaluation metrics for the skin and the organs

For evaluation of the skin registration error, the Euclidean point to surface distance was employed. Note that this experiment was performed with a net density of skin correspondences that was appropriate for the torso and therefore the calculated surface distance does not include the limbs.

To assess the organ interpolation performance, the Dice coefficient s [81] was computed. This measure takes two individual absolute volumes V_1 and V_2 as well as their overlap into account and is defined as follows:

$$s = 2 \frac{|V_1 \cap V_2|}{|V_1| + |V_2|} \tag{3.6}$$

The stomach, spleen and intestines were not considered for determining dice coefficients, because of the large environmentally dependent variability in shape and location.

All experiments were run using Matlab 2007b (The Mathworks, Natick, USA). The time requirements are ≈ 3 mins for the data preprocessing and the articulated skeleton and lungs registration, ≈ 3 mins for calculating the geodesic distances and ≈ 3 mins to determine the dense landmark correspondences on the skin and warping the organs.
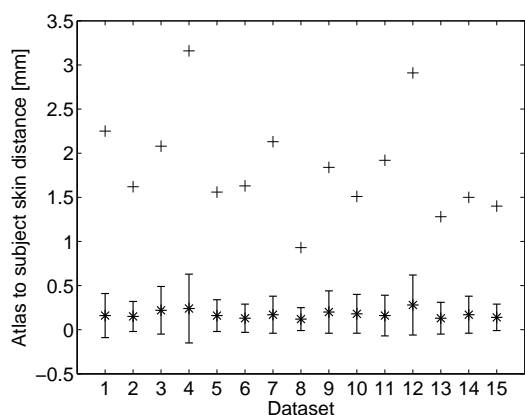
Figure 3.12: The mean atlas to surface distance after registration for the contrast-enhanced datasets. Maximum values are indicated with plus signs. (1voxel$\hat{=}$214 μm).
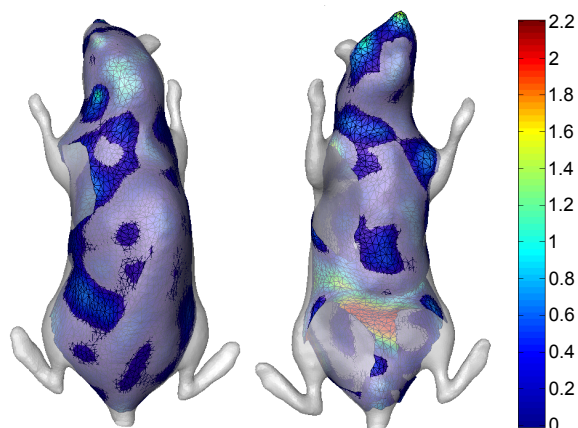
Figure 3.13: An original (gray) and an approximated animal skin. The colorcoding represents the Euclidean distance between the two surfaces (units in millimeters).

3.4 Results

3.4.1 Skeleton and lung registration

In all 26 cases, the matching converged to a correct solution from the automatically estimated initial position. Fig. 3.9 shows several examples of animals in prone and supine position. The Euclidean point to point distance between the manually defined joint locations and the ones determined by the articulated bone registration is shown in Fig. 3.10. The boxplots show the lower quartile, median and upper quartile values. The whiskers extend within 1.5 times the interquartile range. Outliers are indicated with a plus sign.

The mean Euclidean point to surface distance between atlas and subject skeleton surfaces decreases from 2.93 ± 0.63 mm to 0.58 ± 0.04 mm and between the lungs surfaces from 1.76 ± 0.49 mm to 0.42 ± 0.07 mm, including all 26 cases.

3.4.2 Skin registration and organ interpolation

In 4 out of the 15 contrast-enhanced datasets, the automated skeleton initialization was incorrect, and required manual correction. The subsequent hierarchical matching succeeded in all cases given a manually corrected initialization. The mean Euclidean point to surface distances between atlas and subject torso after registration for all 15 datasets are presented in Fig. 3.12. Fig. 3.13 gives an indication of the distribution of the error over the surface. The volumes of the manually segmented and the approximated organs as well as the calculated Dice coefficients are given in Fig. 3.14. Qualitative examples of the skeleton registration and subsequent organ interpolation are shown in Fig. 3.15 and Fig. 3.16.
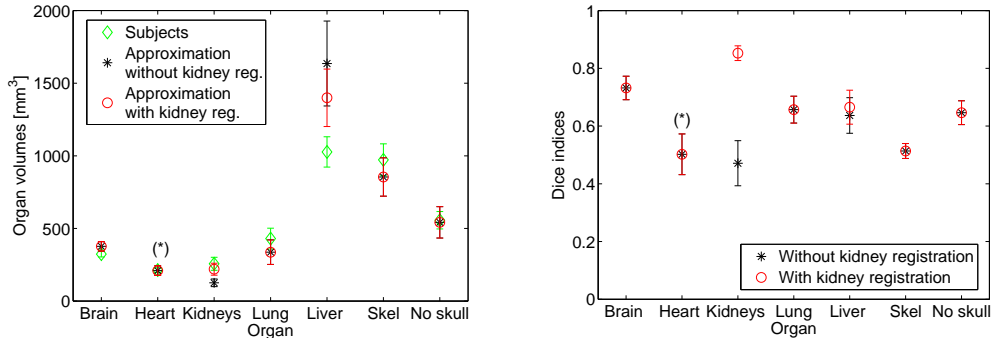
Figure 3.14: Mean value and standard deviation of the organ volumes (left) and the Dice co-efficients (right). The Dice coefficient for the skeleton is given with and without including the skull. Additional results are given if the kidneys are registered as well (see 'Discussion'). For the brain, heart, lungs and the skeleton, the results are identical with or without kidney registration. (*) The result is based on a subset of the data (see text).

3.5 Discussion

The experiments demonstrate that the method performs highly robust in the presence of large postural variations, with successful fully automated matching in 37 out of a total of 41 cases. In the remaining 4 cases, only the initial animal pose estimate required manual correction. The achieved accuracies are discussed in the following.

3.5.1 Skeleton and lungs registration

Using articulated registration, a mean surface distance between the atlas and the target skeleton and lungs within two voxel dimensions is accomplished and we show that the method can handle bones with moderate osteolysis. This performance, given the large variety in the data with respect to posture, strain, gender and size of the animals, demonstrates the robustness of the method. The results are comparable to the accuracy reported in [26]. However, our approach is more than an order of magnitude faster.

An important fact to notice is that there exists a clear dependency between the mean surface distance and the joint location distance before the registration: the lower the bone or the joint in the hierarchy, the larger the distance. The dependency does not appear anymore after the registration (Fig. 3.11). This is an indication that possible registration errors made at a high hierarchical level do not propagate down the tree and do not influence the registration result of elements at a lower hierarchical level. For all joints, the joint localization error decreases an order of magnitude as a result of the registration.

Although it appears from Fig. 3.10 that the joints of the front limbs could be determined significantly less accurate than the hind limbs (balanced one-way ANOVA $p < 0.05$). This is caused by the fact that the hind limbs are modeled as rigidly connected to the pelvis, whereas the front limbs are modeled as dependent on the skull registration only (without a rigid connection). As a result, the front limbs are occasionally placed

Top view   Bottom view

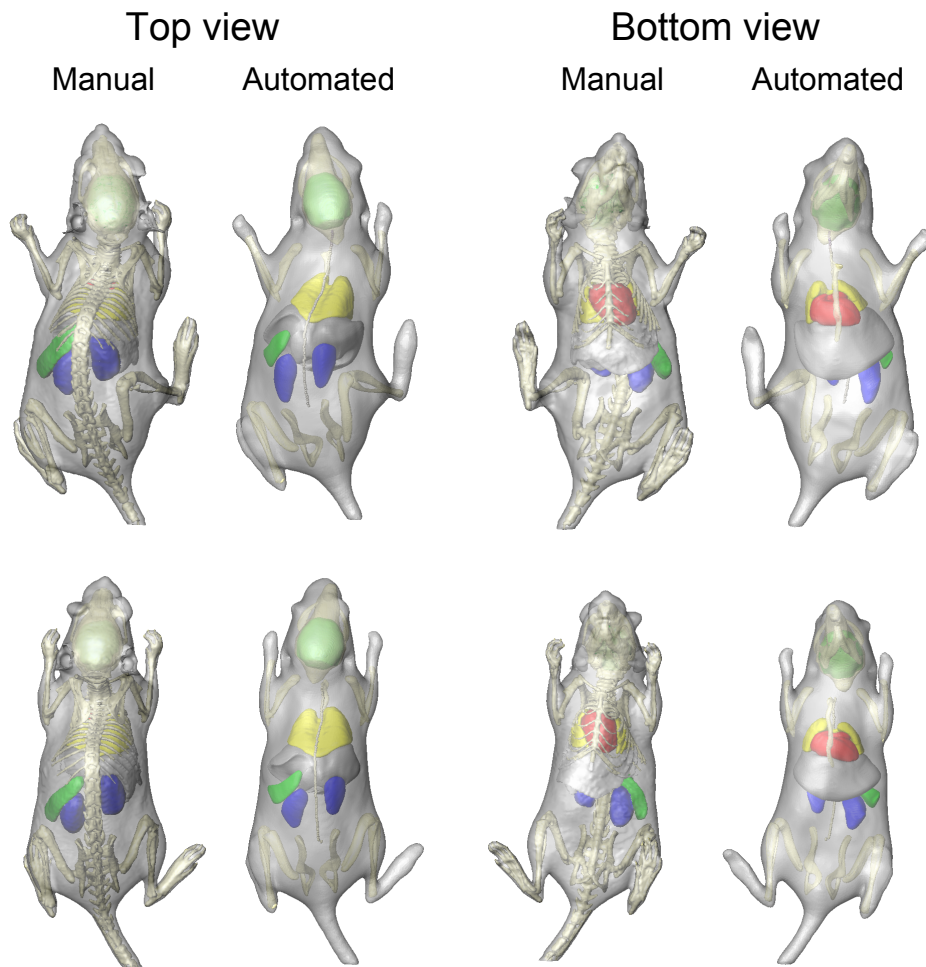Manual   Automated   Manual   Automated

Figure 3.15: Skeleton registration and organ interpolation result for two different mice (top and bottom row). The rows show alternately the manually segmented animal and the mapping result. Only those objects are shown that are used for calculating the Dice coefficients (except of the spleen and the skin).

relatively further away from their target after initialization. In such a situation, the final registration result may be suboptimal. There are no significant differences among the hind limbs and among the front limbs themselves.

Another situation where suboptimal registration results can occur is when two adjacent long bones are pointing in almost the same direction or the opposite direction (meaning that they are almost aligned next to each other). In some of these cases, the resulting scaling factor along the longitudinal bone axis was the maximum value that was considered anatomically realistic for this particular bone (scaling by 15%). As a result, parts of the adjacent bones were erroneously assigned to belong to the target bone during registration. These cases are shown as outliers in Fig. 3.10. A remedy for this problem would be to register adjacent bones simultaneously or to traverse the hierarchical tree several times. The previous registration result could be used for initialization.

3.5.2 Skin registration

As presented in Fig. 3.12, the mean surface distance between the atlas and the subject skin is in the order of one voxel dimension. This indicates that the chosen amount of correspondences, together with the minimum and maximum geodesic distance constraints and the regularization parameter λ result in a proper interpolation of the surface while surface smoothness is retained (Fig. 3.13).

There are some areas on the surface where the surface distance becomes larger (red areas in Fig. 3.13). In these areas there are either not enough skin correspondences available because they are too far away from bone, or the automatically extracted subject surface contains elements that are not included in the model skin (eyes). In applications where a high accuracy particularly in the lower abdomen is needed, the minimum and maximum geodesic distance constraints should be defined for all the correspondences individually instead of using the same values for all of them. This would allow to better deal with the area specific density of the initial sparse landmarks on the skin. Another advantage would be that the amount of candidates around already found correspondences could be drastically reduced in areas with dense initial landmarks. Another way to improve the accuracy of the skin interpolation would be to assume the landmark localization errors on the skin to be non-isotropic i.e. to allow shifting correspondences only tangential to the surface [111] during TPS interpolation.

3.5.3 Organ interpolation

For the soft tissue interpolation step we only considered the animal torso and therefore derived a coarse net of correspondences. To include surface areas that have a large curvature like the limbs as well, determination of corresponding nodes should start at a coarse scale (in terms of intervertex distance) and, depending on the required amount of detail, continue at a smaller scale, e.g. as proposed in Wang *et al.* [108]. This however is only feasible, if the model is detailed enough. Furthermore, the limbs should not touch each other or the torso since the calculated geodesic distances may be wrong in such a case.

The calculated Dice coefficients of volume overlap indicate the feasibility of the presented soft tissue interpolation but in addition show some limitations of the method. Since the interpolation does not distinguish between stiffness properties of different tissue types, all the organs are treated in the same manner. This means that in areas where the shape differs most between the atlas and the subject, typically the abdomen, organs may deform in a way that is anatomically not realistic. An example are the kidneys, which may be squeezed and underestimated up to half of their actual volume after warping (Fig. 3.14). As a result, the Dice coefficient is smaller for the kidneys.

Although the Dice coefficients for the registered objects i.e. the skeleton (and as a result the brain) and the lungs are high as expected, they are limited by the fact that the volumes for both are systematically underestimated. The reason for this is that the preprocessing of the CT data causes all parts of the joints to be represented as bone. Especially in the knee and the ankle joints this leads to an overestimation of the bone volume. As for the lungs volume, its underestimation is the result of a simplified

Coronal (Kidneys) Coronal (Heart) Sagittal
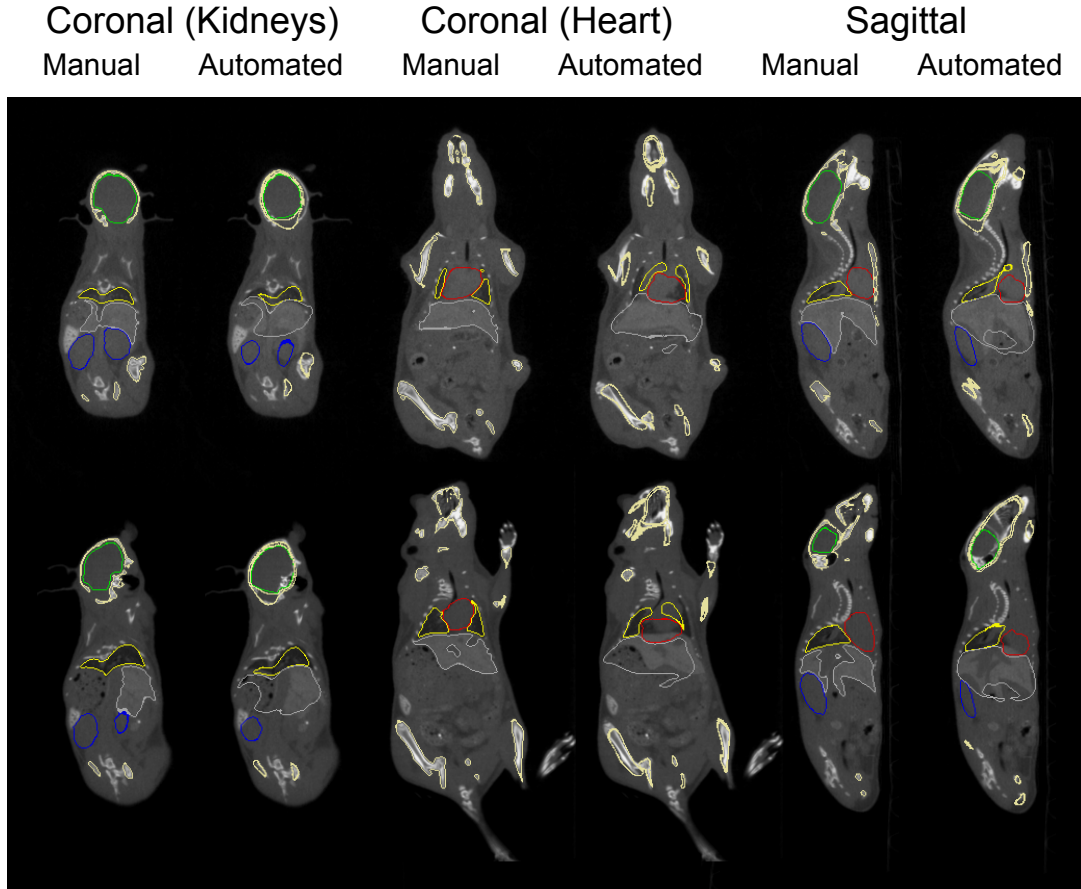Manual Automated Manual Automated Manual Automated

Figure 3.16: Comparison of manual bone and organ contours of two different mice (top and bottom row) in contrast-enhanced MicroCT data. Each row shows alternately the result of the manually drawn contours and the estimated contours for two coronal planes and one sagittal plane. Note that the contrast is only used for delineation of the organs and not for registration.

representation of the lungs in the atlas.

Triggered by the large difference in volume between the subject and atlas liver, we designed an experiment to further investigate on the influence of the shape simplifications in the atlas for this particular organ. Since the liver is adjacent to the lungs and the kidneys we aimed on defining as many correspondences as possible on these two organs before the mapping. The lungs are already registered and therefore a dense landmark set can easily be obtained. As for the kidneys we decided to integrate them into our hierarchical framework (on $L3$). Since we do not expect large shape variations among healthy subjects, allowing 9 DoFs as for the bones suffices to approximate intersubject shape differences. The target kidneys were segmented manually as described in section 3.3.2. The experiment was performed using the 15 contrast-enhanced datasets. The effect on the organ volumes and the Dice coefficients is shown in Fig. 3.14. After registration, the measured kidney volume is almost the same as the target volume and the Dice coefficient has increased. As for the liver, the volume has decreased but is still significantly different from the target (paired t-test $p = 5.5e^{-07}$). From this we conclude that the model

simplifications are the prominent limiting factor of the interpolation result for the liver. Further investigation using an improved animal model has to be conducted to be able to clearly distinguish between segmentation inaccuracies because of model simplifications and physiological intersubject variability.

3.5.4   Segmentation accuracy

The registration of the skeleton was achieved with high accuracy and enables to accurately segment individual bones of the skeleton from the data. For applications that require a higher accuracy e.g. to assess morphological bone changes locally, the amount of DoFs for the articulated registration of the skeleton should be increased i.e. the transformation model should include nonlinear deformations as well. To render the registration robust to large postural variability, the results of our method could serve as an initialization.

Compared to the results for the skeleton and lungs, the segmentation accuracy for the abdominal organs is restricted. However, it is still high enough for anatomical referencing or to provide a heterogeneous tissue model for Bioluminescence Tomography, because even a coarse segmentation can significantly improve the reconstruction result [9, 91]. A possibility for improvement would be to use our result as an initialization of a nonrigid, voxel-based registration method for the entire body. This would require sufficient soft-tissue contrast in the data. However, in many routine MicroCT studies, contrast agents (e.g. eXIA and Fenestra), highlighting abdominal organs, are not part of the experimental protocol.

3.6   Conclusion and Future Work

This paper presents a fully automated method for atlas-based whole-body segmentation in non-contrast-enhanced MicroCT. We proposed a solution that divides the problem into an atlas constrained registration based on high-contrast organs in MicroCT (skeleton, lungs and skin) and a soft tissue approximation step. Experiments demonstrated the method's effectiveness to overcome exceptionally large variations in posture and shape, even in the absence of soft tissue contrast in *in vivo* MicroCT data. By combining an articulated skeleton with a hierarchical anatomical model and a suitable registration framework for individual bone elements (ICP), a final registration result could be obtained very time efficient but yet with high accuracy (between one and two voxel dimensions). We also showed the robustness of the method with respect to moderate bone resorption. In addition, the presented performance of the organ approximation proved that the missing soft tissue contrast in the data can be compensated for and the results of the calculated Dice coefficients outperform previously reported results [20].

To our knowledge, there are no reports to date of other unsupervised methods that can deal with such a high variability in posture and shape and that have been validated as extensively as in this work.

The method is suitable for intrasubject as well as intersubject registration using data acquired *in vivo* and is applicable for referencing of internal processes in molecular imaging research. The absence of any user interaction to initialize the procedure would make

this method suitable for high-throughput batch processing, and posterior result checking and occasional manual initial pose correction. Above that, it could serve as a way to provide a whole-body heterogeneous tissue model for bioluminescence tomography.

The method was tested using whole-body data of mice only but would be applicable to other animals as well, if an atlas is available. Besides that, we want to point out that not only data of entire animals but also data including only parts of an animal can be handled by simply removing the missing body parts from the hierarchical anatomical model. The determination of skin correspondences and the organ mapping can in principle be restricted to a certain volume of interest as well.

In the future we plan to develop multiple small animal models and investigate how to minimize the influence of shape differences between the model and the target, especially in the organ interpolation step. We also plan to generalize the whole-body registration to other modalities as well. The focus will not only be on volumetric data (MRI or SPECT) but also on photographs from the subject surface (mono- or biplanar) for posture estimation, using skeleton based motion constraints.

The modified MOBY atlas is publicly available in the 'Downloads' section at `http://www.lkeb.nl`.

Acknowledgements

Appendix

Calculation of geodesic distances

To determine geodesic distances on the skin surface, the Fast Marching Algorithm [113] is used, a very time efficient method to solve the Eikonal equation $|\nabla T| = F(\mathbf{x})$ using triangulated domains. Given a starting point $\mathbf{x}$, a front with speed F is expanded on the mesh and arrival times T can be determined for all other vertices. By setting a constant propagation speed $F = 1$ all over the mesh, the arrival times are equal to the geodesic distance between the starting point and a given endpoint. The fact that the accuracy of the derived geodesic distances depends on how dense the mesh is sampled requires analyzing the calculation error in practice for the application at hand. For the underlying problem, the target surface is represented with 2000 nodes, which is sufficient to represent the major deformations that are caused by postural variations. Experiments showed that, given a starting point, the mean error for determination of geodesic distances to nodes within a given range g_{max} is below one voxel dimension. Therefore, the chosen sampling is a good tradeoff between calculation time for the geodesic distances
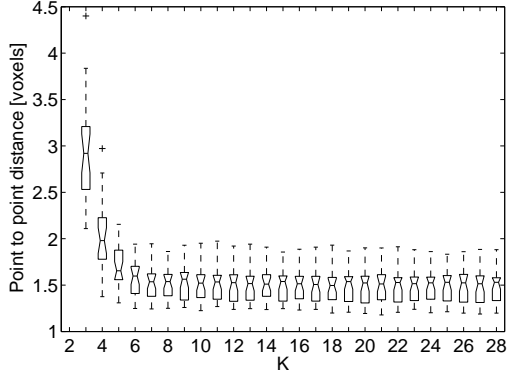
Figure 3.17: Median distance between the subject surface and the mapped atlas surface for 26 subjects, depending on the parameter K (see text). Note that the point to point rather than the point to surface distance is presented here.
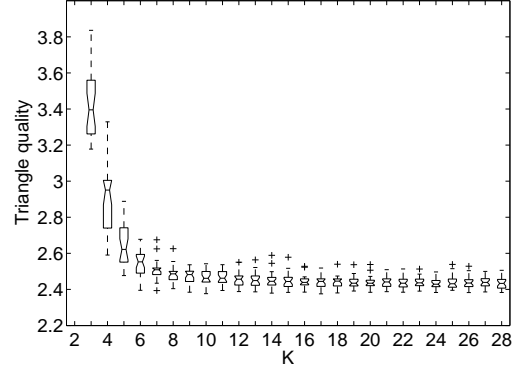
Figure 3.18: Median triangle quality of the mapped surfaces, depending on K. The median quality of the atlas skin triangles before the mapping is 2.28.

and possible correspondence localization accuracy. Note that the geodesic distances have to be calculated for each target but only once for the source (atlas) surface. Therefore the atlas skin surface can be sampled very densely and the distribution of geodesic distances be calculated offline.

Optimum value determination for parameter K

To derive the optimum value for the parameter K we chose $g_{min} = 15$ and $g_{max} = 50$ and varied K within a range of 2 and 28. For this experiment, we used the skins of all animals of the non-contrast-enhanced study (26 animals). Quantification of the performance is based on the median point to point distance between the source (atlas) and the target skin surface, after determining correspondence and mapping the atlas torso to the target surface, a triangle quality measure, applied to the mapped atlas surface and the processing time. The triangle quality is defined as the ratio of the radius of the circumcircle and the radius of the incircle of a triangle (a value of 2 is the optimum). Fig. 3.17, Fig. 3.18 and Fig. 3.19 show the results of the experiment. The boxplots indicate, that $K = 8$ is a reasonable choice and a good tradeoff between accuracy and calculation time, since neither the surface distance nor the triangle quality improve significantly for $K > 8$.

Invertiblity of the Thin Plate Spline transformation

To investigate if the regularization of the energy functional (section 3.2.5) leads to an invertible transformation, given a dense set of skin and skeleton correspondences (section 3.2.4), we calculate the determinant of the Jacobian of the final transformation for all 26 datasets that were used for the skeleton registration validation. The determinant was determined in steps of 180 μm (twice the phantom voxel size) i.e. in a total vol-
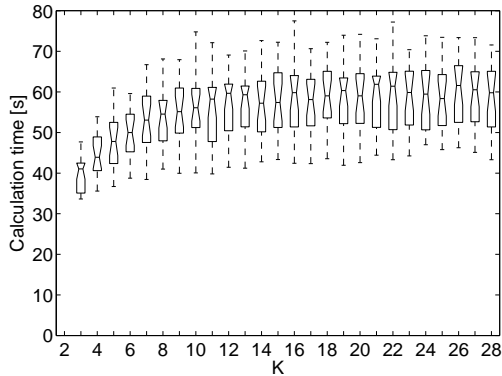
Figure 3.19: The calculation time for determining skin correspondence for 26 subjects, depending on K.
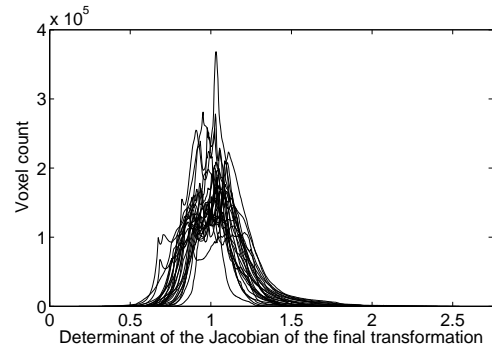

Figure 3.20: Histograms of the determinant of the Jacobian of the final transformations for all 26 datasets used for validating the skeleton registration.

ume of $201 \times 201 \times 601$ voxels and was based only on the non-affine parts of the final TPS transformations. Figure 3.20 shows the results. The first observation is that all values are positive, proving that the transformation is in principle invertible. Second, the vast majority of the determinants lie between 0.5 and 1.5. This means that only moderate expansion and compression takes place (1: neither compression nor expansion, <1: compression, >1: expansion [114]).

Atlas-Based Whole-Body Segmentation of Mice from MicroCT data